

Zhigang Zhang<sup>1</sup>, Zedong Wu<sup>1</sup>, Zhiyuan Wei<sup>1</sup>, Jiawei Mei<sup>1</sup>, Rongxin Huang<sup>1</sup>, and Ping Wang<sup>1</sup><https://doi.org/10.1190/tle42030207.1>

## Abstract

Full-waveform inversion (FWI) has become the centerpiece of velocity model building (VMB) in seismic data processing in recent years. It has proven capable of significantly improving the velocity model and, thus, the migration image for different acquisition types and geologic settings, including complex environments such as salt. With the advent of FWI imaging, the scope of FWI applications has extended further from VMB into the imaging landscape. However, current FWI applications in the industry prevalently employ the acoustic approximation. One common problem of acoustic FWI (A-FWI) is the apparent salt halos at the salt-sediment interface in the resulting FWI velocity and FWI image, the presence of which hinders direct interpretation and imaging focusing around salt bodies. With synthetic and field data examples, we demonstrate that this salt halo is caused mainly by the large mismatch between the elastic recorded data and the acoustic modeled data, particularly at middle to long offsets. To overcome limitations imposed by acoustic assumptions, we developed an elastic FWI (E-FWI) algorithm that combines an elastic modeling engine with the time-lag cost function, which we call elastic time-lag FWI (E-TLFWI). With a more accurate modeling engine, E-TLFWI significantly reduces the salt halo observed in its acoustic counterpart. However, we also observe that the images migrated using the A-FWI and E-FWI velocity models remain similar overall, with some slight improvements around and beneath salt boundaries, particularly near steep salt flanks, as a result of the reduced salt halo. By contrast, FWI images derived from E-TLFWI show considerable benefits over those from acoustic time-lag FWI, such as improved event focusing, better structural continuity, and higher signal-to-noise ratio. The sharpened salt boundaries and enhanced quality of the FWI images reveal the significant value of E-FWI and provide the justification for its greatly increased cost.

## Introduction

Historically, salt velocity model building (VMB) has relied heavily on manual interpretation and scenario tests, which are known to be time consuming, labor intensive, and highly prone to human misinterpretation. As a result, subsalt images often remain very poor in areas where the salt geometry is complex, even after strenuous efforts. Since originally proposed by Lailly (1983) and Tarantola (1984), full-waveform inversion (FWI) as a data-driven approach has been considered the holy grail for automatically solving the VMB problem with complex structures. Only recently, however, has FWI realized this potential of automatic velocity model updates in salt settings, with significantly

improved subsalt images regardless of input data type and geologic setting (Michell et al., 2017; Shen et al., 2017; Zhang et al., 2018; Nolte et al., 2019; Wang et al., 2019).

Velocity models conventionally have been perceived as the low-wavenumber components of the earth model, as in Claerbout's diagram (Claerbout, 1985). It is migration that takes a known velocity model and processed input data to produce reflectivity images, the high-wavenumber components of the earth model. However, migration algorithms generally use adjoint modeling operators to approximate the inverse of the forward modeling. Consequently, migration images often suffer from migration artifacts and uneven illumination (Claerbout, 1992). To overcome this drawback, least-squares migration (LSM) has been proposed to approximate the inverse of the forward modeling operator through a linear inversion problem (assuming an accurate velocity model) and consequently reduce migration artifacts and compensate for uneven illumination (Baysal et al., 1983; Schuster, 1993; Nemeth et al., 1999; Wang et al., 2016). Unfortunately, in complex areas where the illumination is too low and/or the velocity model has relatively large errors, LSM often shows limited efficacy. Another way to improve illumination is to utilize the multiple energy in the input data that is discarded in primary-based migration approaches. Different flavors of multiple migration and least-squares multiple migration have been proposed to take advantage of the extra illumination (Liu et al., 2010; Lu et al., 2011; Wong et al., 2014; Yang et al., 2015). However, such approaches often suffer from crosstalk noise while still discarding some valuable information in the recorded data, such as diving waves. By contrast, FWI imaging naturally handles these issues by employing the full-wavefield data as the input and by utilizing a nonlinear least-squares process to derive velocity and reflectivity in one go (Zhang et al., 2020; Huang et al., 2021). This approach not only simplifies the seismic processing workflow significantly, it also produces much better images that conventional migration and LSM cannot rival. Furthermore, unlike most VMB tools that can only resolve low-wavenumber components, FWI can readily reveal high-wavenumber components of the subsurface velocity by proceeding toward high frequencies. This is crucial for focusing complex wavefields including multiple scattering in FWI imaging that demands highly accurate model kinematics (Wei et al., 2021).

Despite the fact that FWI has gained tremendous popularity in the industry, most of its applications are based on the acoustic formulations for three main reasons: (1) elastic modeling is substantially more compute-intensive than acoustic modeling; (2) it is still very challenging to obtain good shear-wave velocity ( $V_s$ ) models for elastic FWI (E-FWI); and (3) acoustic modeling can

<sup>1</sup>CGG, Houston, Texas, USA. E-mail: zhigang.zhang@cgg.com; zedong.wu@cgg.com; zhiyuan.wei@cgg.com; jiawei.mei@cgg.com; rongxin.huang@cgg.com; ping.wang@cgg.com.

explain most events in the recorded data and typically produce decent acoustic FWI (A-FWI) velocities and FWI images.

Still, the elastic effects in the recorded data leave their marks. One well-known example is the salt halo with a significant length scale that cannot be explained by the limit of the inversion frequency (Wu et al., 2022). This phenomenon can be demonstrated by a synthetic example using the BP 2004 velocity model (Billette and Brandsberg-Dahl, 2005) in Figure 1. When running A-FWI up to 10 Hz using the acoustic input data, the salt boundary is properly resolved (Figure 1b). Conversely, if we switch to elastic input data and still run A-FWI up to the same frequency, a larger salt halo can be observed in the output velocity model, which smears the salt boundary and contaminates the sediment and salt velocity around the salt body (Figure 1c). Furthermore, crosscutting artifacts can be observed in the sediment area, which reduces the signal-to-noise ratio (S/N) of the inverted model. Mora and Wu (2018) use synthetic examples to demonstrate that acoustic inversion of large-offset data could have slow convergence because of the difficulty of acoustic modeling in matching the recorded data with strong elastic effects. There are studies that propose preprocessing input data to remove the elastic effects, for example by a data-matching approach between elastic and acoustic modeled data (Agudo et al., 2020). Nevertheless, this is a challenging task and cannot be done perfectly, especially when the wavefield is complex.

### Elastic time-lag FWI

Ideally, the elastic wave equation should be included in FWI to account for the elastic effects, particularly for long-offset data in the presence of large impedance contrasts (Plessix and Krupovnickas, 2021). To incorporate the elastic effect, Wu et al. (2022) combine an elastic modeling engine with the full 21 elastic moduli and a time-lag cost function that is proven to be effective in stably improving velocity models and images in different geologic settings (Zhang et al., 2018; Wang et al., 2019). The synthetic data example using the BP 2004 model shows that, unlike its acoustic counterpart, elastic time-lag FWI (E-TLFWI) can properly handle elastic input data and thus construct a decent salt boundary as expected (Figure 1d). This indicates that the salt halo observed in the A-FWI velocity model is caused by unaccounted elastic effects in the input data.

In the next sections, we examine the effectiveness of E-TLFWI with two ocean-bottom-node (OBN) data sets and one

towed-streamer data set. All these examples confirmed that the salt halo observed on the A-FWI velocity model can be greatly reduced by E-TLFWI. Moreover, while reverse time migration (RTM) images using A-FWI and E-FWI models are overall qualitatively comparable, except at locations around and beneath complex salt bodies, the E-FWI images exhibit convincing uplifts compared to their acoustic counterparts, with improved event focusing, better structural continuity, and higher S/N.

### Field data examples

**Atlantis OBN in the Gulf of Mexico.** The Atlantis Field is one of the largest oil fields discovered in the Gulf of Mexico (GoM), lying directly below the Sigsbee Escarpment. A significant portion of the field is shadowed by a complex allochthonous salt body with several thin salt fingers pinching out over the crest of the reservoir. Faulting within the subsalt reservoir further increases the imaging challenge. An OBN data set was acquired with the aim of facilitating VMB in addition to its normal reservoir monitoring task (Lewis et al., 2016). The data set has decent S/N for low frequencies down to 1.5 Hz and long offsets up to 30 km. Acoustic time-lag FWI (A-TLFWI), starting from a smoothed legacy model built by the conventional workflow, was able to correct salt misinterpretation and delineate the sediment velocity close to the salt body. The A-TLFWI updated velocity model led to considerable improvements in the RTM image. FWI imaging, empowered by iterative least-squares data fitting of the full-wavefield data, further improves the event continuity and amplitude balance as well as reducing migration swings and noise (Huang et al., 2021). Yet, there is a considerable salt halo in the A-TLFWI model and FWI image even after driving the inversion frequency up to 18 Hz, which poses a problem for direct interpretation around salt bodies (Figures 2a and 2d). As indicated by the earlier synthetic examples, this salt halo is due to the missing elastic effects in the A-TLFWI. As expected, E-TLFWI at the same frequency reduces the span of the salt halo and the ambiguity of the salt-sediment boundary (Figure 2b). Furthermore, the E-TLFWI velocity model shows clearer velocity contrasts and more details in the sediment and subsalt areas. The resulting E-FWI image has improved event continuity and S/N throughout the entire section (Figure 2e). When running to an even higher frequency, 25 Hz, E-TLFWI further sharpens the image, including the salt boundary, and reveals fine structures that are not resolved in the 18 Hz velocity model and FWI image (Figures 2c and 2f). On the depth slice,

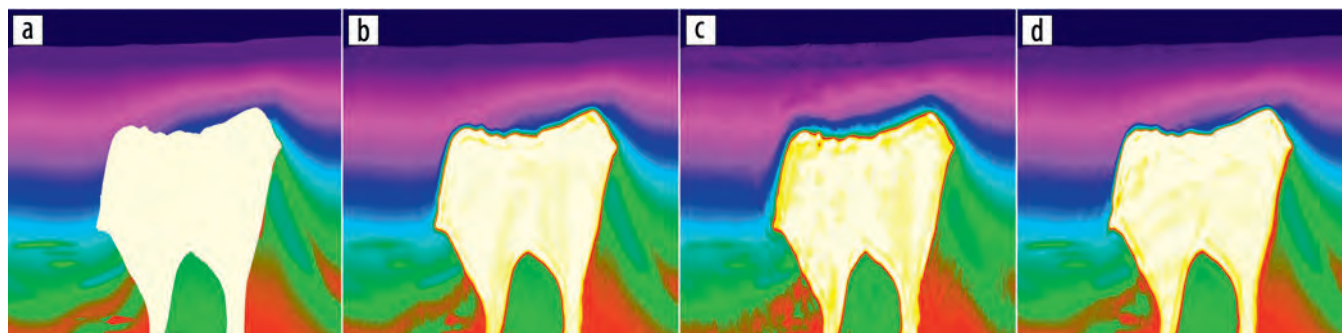
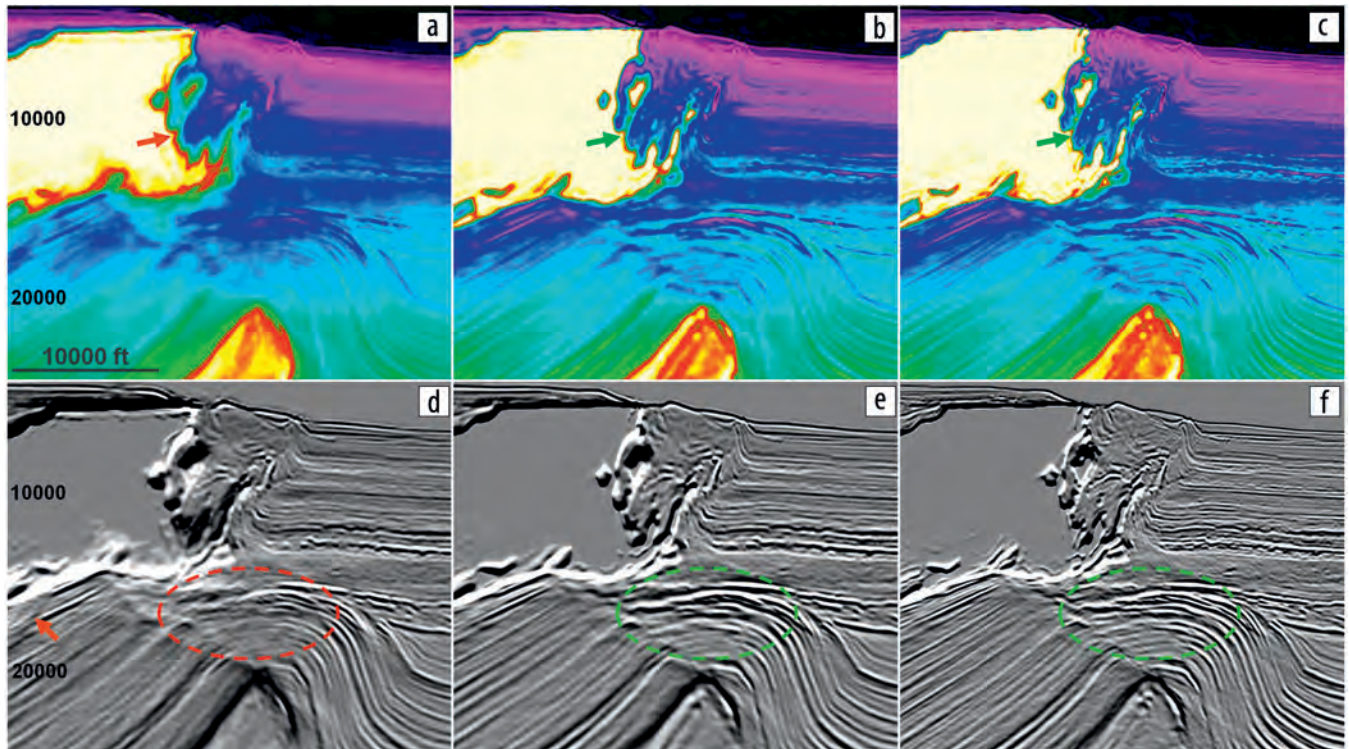


Figure 1. (a) True model. (b) A-TLFWI model with acoustic input data. (c) A-TLFWI model with elastic input data. (d) E-TLFWI model with elastic input data.

a sharper salt boundary and more clear-cut faults can also be observed in the E-FWI image (Figure 3c) compared to the A-FWI image (Figure 3b). The events from an open basin to the subsalt area (highlighted by the green circle and arrows) show more consistent amplitudes and higher S/N.

**Herschel OBN in the GoM.** The Herschel Field sits within the giant Na Kika oil and gas field in Mississippi Canyon in the GoM, located approximately 140 miles southeast of New Orleans, Louisiana, USA. Salt at the Herschel Field has an hourglass shape with a salt diapir in the shallow section that connects by steep salt flanks all the way to the autochthonous Louann salt in the deep section. The low impedance contrast with the surrounding

high-velocity Cretaceous carbonate at the deeper section makes it challenging to delineate the salt boundaries in seismic images. Sedimentary layers at the Herschel Field feature high-dipping Cenozoic truncations against salt flanks, and faulted Mesozoic sediment is deposited on the deep Louann salt. The field occurs in a three-way closure with a major fault down to the northwest and steeply updipping sediment truncations against a salt flank. Although the acquired OBN data had limited offset coverage, a maximum of approximately 12.5 km, A-TLFWI provides good kinematic updates and captures detailed velocity features around the Norphlet Formation at 9–10 km depth (Yao et al., 2020). However, there is still an apparent salt halo in the A-TLFWI



**Figure 2.** Section view of Atlantis OBN data: (a) 18 Hz A-TLFWI velocity model, (b) 18 Hz E-TLFWI velocity model, and (c) 25 Hz E-TLFWI model; (d) 18 Hz A-TLFWI image, (e) 18 Hz E-TLFWI image, and (f) 25 Hz E-TLFWI image. The E-TLFWI velocity models exhibit sharpened salt boundaries and improved details in sediments, and the corresponding E-TLFWI images show better-defined salt boundaries and improved focusing and S/N.

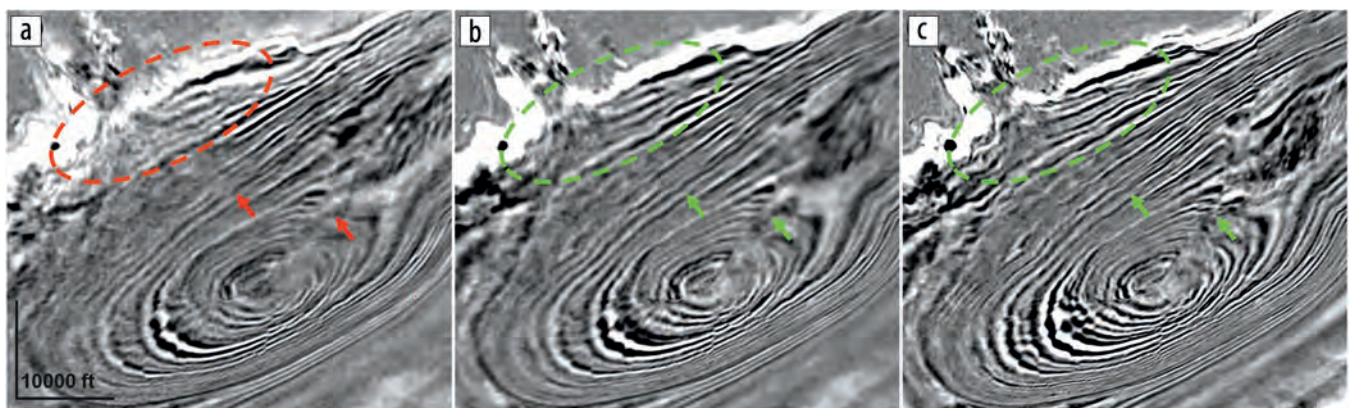


**Figure 3.** Depth view of FWI images from Atlantis OBN: (a) 18 Hz FWI image from A-TLFWI, (b) 18 Hz FWI image from E-TLFWI, and (c) 25 Hz FWI image from E-TLFWI. The E-TLFWI images show improved continuity, higher S/N, and better-defined faults than the A-TLFWI counterpart.

velocity model, even up to 15 Hz (Figure 4a). On the other hand, the salt halo is greatly reduced in the 15 Hz E-TLFWI velocity model (Figure 4c), which again confirms our observations from the previous examples that the missing elasticity is responsible for the strong salt halo in the A-TLFWI velocity model. The sharper salt boundaries both on the top of salt and around the salt flank in the E-TLFWI velocity model can be better seen in the zoomed-in section (Figures 4b and 4d). In addition to the sharper salt boundaries, the E-TLFWI velocity model also shows clearer velocity contrasts and higher S/N in the sediment and subsalt areas (Figures 5a and 5b). Even though the E-TLFWI velocity model is more geologically sensible, the uplift has not translated to clear benefits on the RTM images. The acoustic RTM (A-RTM) images show comparable quality with the A-TLFWI and E-TLFWI velocity models (Figures 6a and 6b). The dim zone below the salt flank with low S/N remains unchanged in the RTM image with the E-TLFWI velocity model. This similar image quality indicates that A-TLFWI has resolved most of the kinematic errors solvable by E-TLFWI in the velocity model, and RTM is not benefiting from the relatively small details captured by the E-TLFWI velocity because it is more susceptible to fundamental issues such as low and uneven illumination. Thanks to the use of the full-wavefield data and the iterative data-fitting process, the A-FWI image has shown significant improvement over RTM with more balanced amplitudes and improved event continuity in the dim zone (Figure 7a). However, even with such improvements, crosscutting noise parallel to the base of salt is still visible in the A-FWI image, and the subsalt events right below the base of salt are smeared and masked by the salt halo. The E-FWI image, on the other hand, reveals the reflectors around and below salt with even more balanced amplitudes, improved continuity, and higher S/N (Figure 7b). On the depth view, the events closer to the salt diapir (highlighted by the ellipses in Figure 8) show

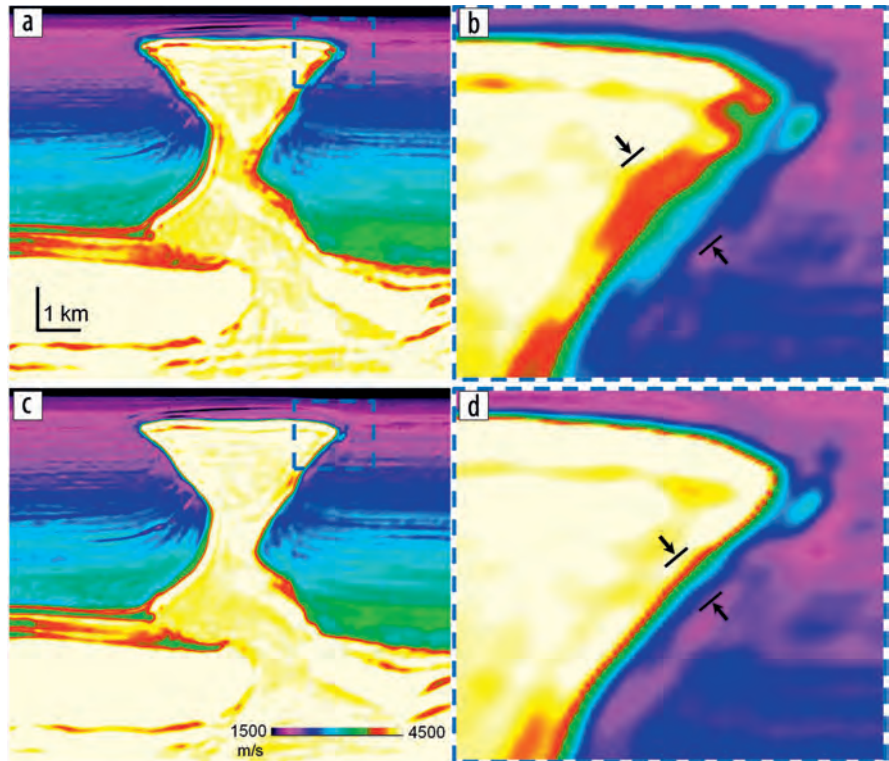


**Figure 4.** Section view of (a) the 15 Hz A-TLFWI velocity model and (b) the zoomed-in display of the blue rectangle in (a); (c) the 15 Hz E-TLFWI velocity model and (d) the zoomed-in display of the blue rectangle in (c). The E-TLFWI velocity model exhibits sharpened salt boundaries and improved details in sediments.

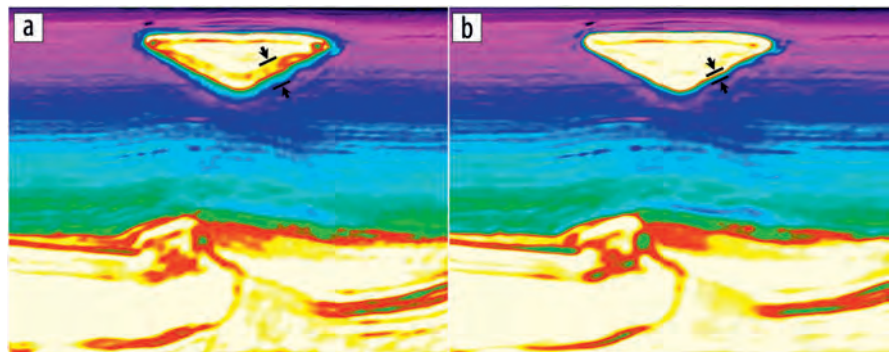


**Figure 5.** Section view of (a) 15 Hz A-TLFWI velocity model and (b) 15 Hz E-TLFWI velocity model. The E-TLFWI velocity model exhibits sharpened salt boundaries and improved details in sediments.

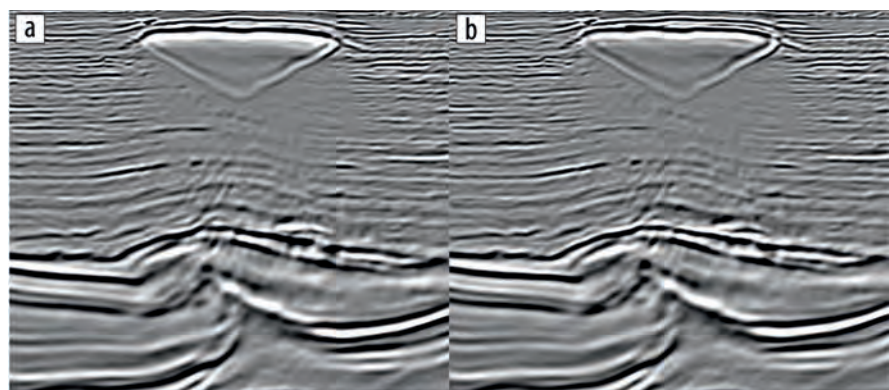


**Figure 6.** Section view of (a) 15 Hz A-RTM image with 15 Hz A-TLFWI velocity model and (b) 15 Hz A-RTM image with 15 Hz E-TLFWI velocity model. The RTM images indicate similar kinematics of the acoustic and elastic velocity models. The image with the E-TLFWI model shows slight improvements in the subsalt area, but the dim zone beneath the salt body remains.

higher S/N and better continuity in the E-TLFWI images than the A-TLFWI images. The faults are also better defined in the E-TLFWI images.

**Walker Ridge towed-streamer in the GoM.** After two OBN data examples, we now examine the effectiveness of E-TLFWI on towed-streamer data, which are less favorable for both VMB

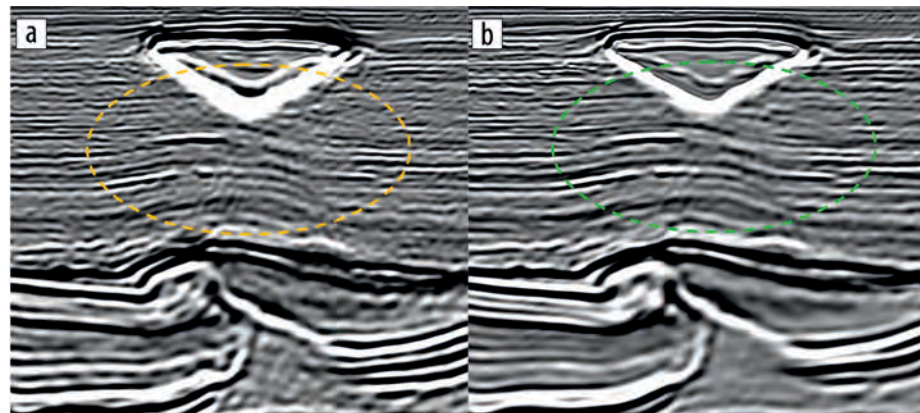


**Figure 7.** Section view of (a) 15 Hz A-TLFWI image and (b) 15 Hz E-TLFWI image. The poor illumination in the subsalt observed on RTM images is largely compensated for on both the A-FWI and E-FWI images. Compared with the A-FWI image, the subsalt events in the E-FWI image have much improved continuity and reduced crosscutting noise.

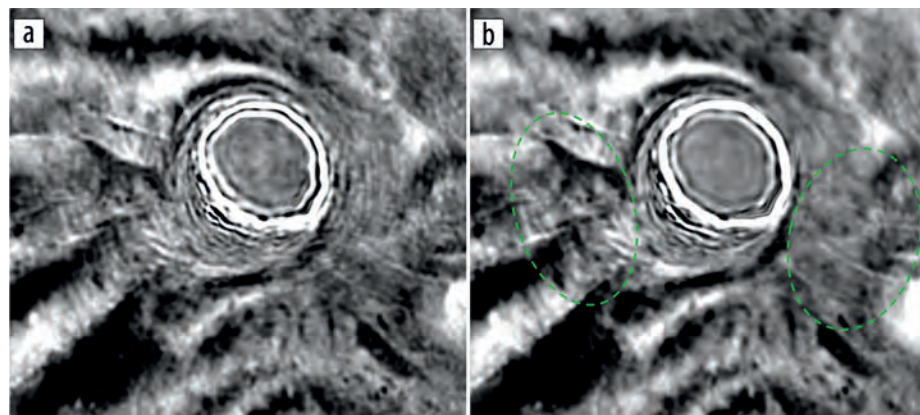


**Figure 8.** Depth slice of (a) 15 Hz A-TLFWI image and (b) 15 Hz E-TLFWI image. The E-FWI image shows better-defined structure and higher S/N than the A-FWI image.

and imaging, around the Monument Field in Walker Ridge, GoM. The Monument Field is in the outer basin of the central GoM, with a subsalt Paleogene sandstone reservoir approximately 9 km below the sea surface. The complicated overburden of low-reflectivity mobile shale bodies and complex salt geometries — which are characterized by steep salt flanks and overhangs, many sutures and inclusions, and multilevel weld systems — poses great challenges to subsalt imaging. Besides the geologic challenges, the existing streamer data are also suboptimal for VMB and deep subsalt imaging owing to its limited maximum offset and azimuthal coverage as well as poor low-frequency S/N. Two streamer surveys, one staggered acquisition, full azimuth from 2013 and one wide azimuth from 2007, were available for this study.

The VMB workflow driven by A-TLFWI adds sediment inclusions, modifies the salt geometry, and thins the weld. It also identifies the slow gas hydrates near the water bottom and the slow shale bodies above the salt weld, which leads to a simplified structure of the salt weld and improved continuity (Figure 9). With the better-resolved overburden and updated salt

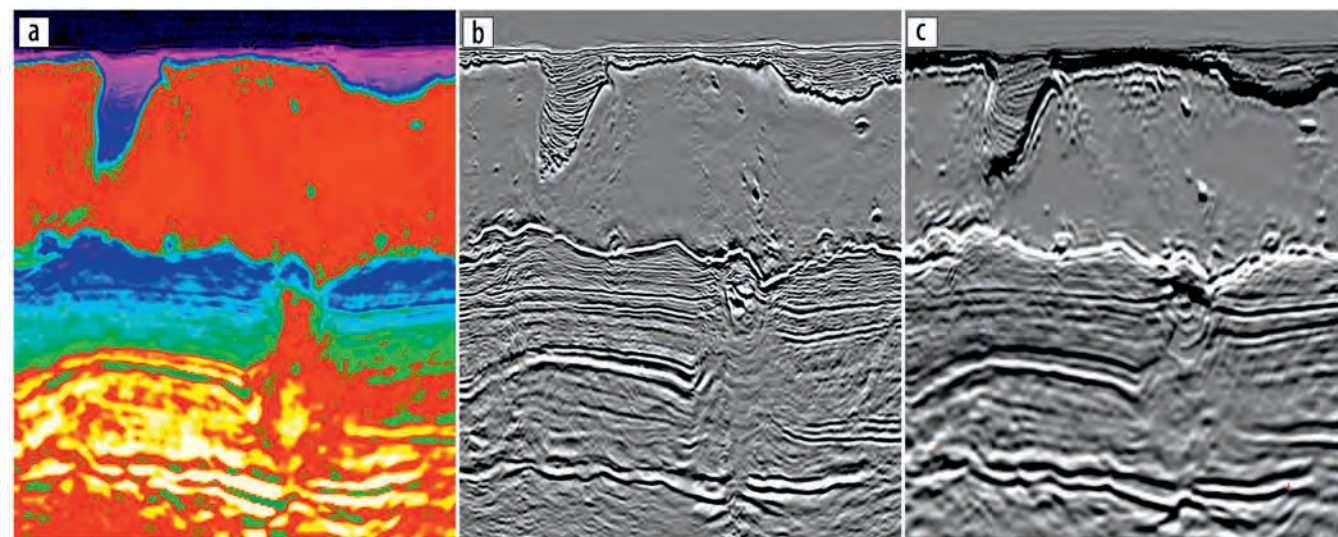


**Figure 9.** Inline section of (a) 8 Hz A-TLFWI velocity model, (b) its 15 Hz A-RTM image, and (c) 8 Hz A-TLFWI image. The FWI image shows improved amplitude balance and higher S/N than the RTM image.

model, the reservoir structure is more geologically plausible, with reduced undulations and improved focusing and continuity (Ren et al., 2022). However, because A-TLFWI cannot properly model the strong elastic effects around salt boundaries with large impedance contrasts, the salt boundary is smeared in the A-TLFWI velocity model (Figure 9a). On the other hand, E-TLFWI effectively reduces the mismatch between synthetic and recorded data in inversion by using an elastic wave propagation engine to simulate the reflection and transmission energy at salt boundaries with better amplitudes and phases. Consequently, the E-TLFWI velocity model renders significantly reduced salt halos along with cleaner subsalt sediment velocity updates in comparison with the A-TLFWI model (Figure 10a). Although some improvements in the RTM image can be observed around and below salt flanks, inclusions, and other locations with large velocity contrasts, the overall comparable kinematics of the acoustic and elastic velocity models deliver similar RTM imaging quality (Figure 10b). The FWI images appear to better exploit the benefits of E-TLFWI than the conventional RTM images. The E-FWI image shows much sharper salt boundaries with greatly reduced halos and more balanced amplitudes, better subsalt event continuity, and higher S/N than its acoustic counterpart (Figure 10c). In particular, the E-TLFWI impressively reduces the noise level in the FWI image, thanks to an improved data match between the elastically modeled synthetic data and the recorded data.

## Discussion

Employing FWI to automatically update the salt model has been the dream of the seismic imaging industry because salt VMB based on manual interpretation and scenario tests is not only time consuming and labor intensive but also largely ineffective. However, FWI has failed to deliver this dream for a long time. Insufficient data, ineffective inversion algorithms, and inaccurate physics were frequently cited as the cause of failure. In particular, the acoustic approximation was once considered as

one of the reasons that FWI failed in salt environments where strong elastic effects exist due to the large impedance contrast at the salt-sediment boundary. In recent years, many field data examples have shown that A-FWI can reasonably update the velocity models in the presence of complex salt bodies and significantly improve subsalt images with different input data sets from OBN data to less favorable wide-azimuth and narrow-azimuth towed-steamer data (Shen et al., 2017; Zhang et al., 2018; Wang et al., 2019). This suggests that the inversion algorithm had been the largest bottleneck for the success of FWI in the salt environment all along, and a good inversion algorithm (particularly the cost function) should be used for A-FWI to mitigate the negative impact of the amplitude discrepancy between the modeled and recorded data. One would hope that E-FWI with an elastic modeling engine could naturally solve the problem of amplitude discrepancy. However, inaccuracies in model parameters (e.g.,  $V_s$  and density), anelastic effects (e.g.,  $Q$ ), and other uncertainties (e.g., source wavelet) could still make the discrepancy between the modeled and recorded data significant, and therefore a good inversion algorithm is similarly required for E-FWI even with a more realistic modeling engine. In other words, the benefits of E-FWI would likely be limited if A-FWI using the same cost function does not work well. Based on the time-lag cost function that has proven to be effective for salt velocity update, we extended our A-TLFWI to E-TLFWI. In addition to the three field data examples shown in this paper, we have applied E-TLFWI successfully to many other field data sets. Here, we share some of the observations from all these applications and attempt to provide some explanations. We then discuss ways to evaluate E-FWI results as well as possibilities to derive additional elastic attributes other than P-wave velocity ( $V_p$ ).

**Observations.** Like the A-TLFWI case, the performance of E-TLFWI is dependent on geology and data type, and the observations vary accordingly. Here, we share some of the consistent observations we have made based on all of our E-TLFWI applications so far:

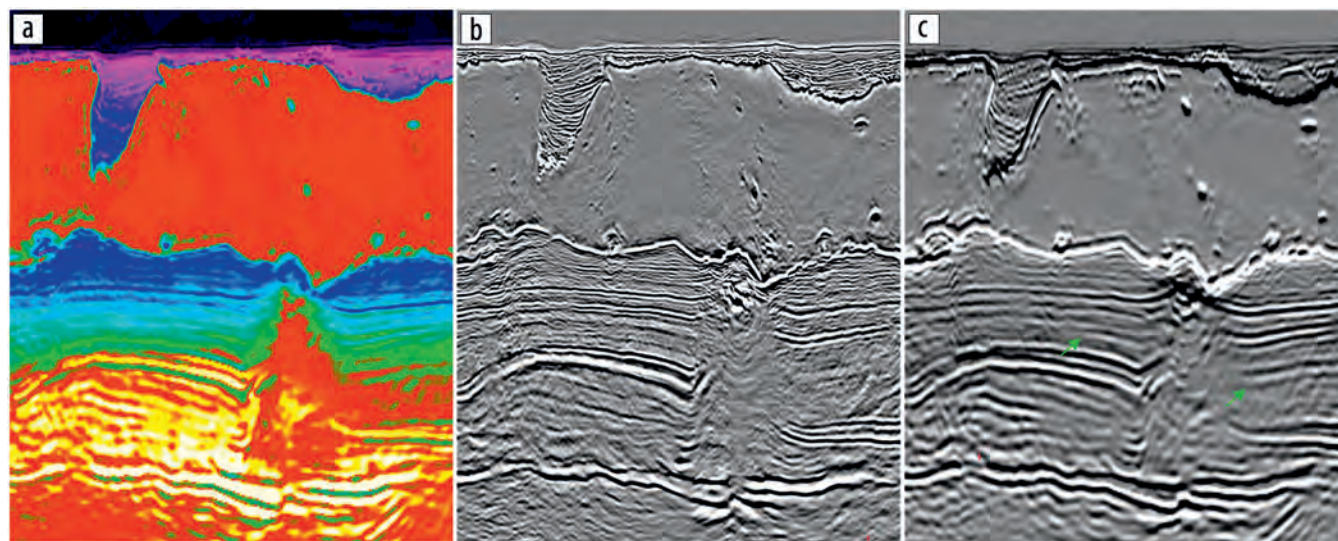


**Figure 10.** Inline section of (a) 8 Hz E-TLFWI velocity model, (b) its 15 Hz A-RTM image, and (c) 8 Hz E-TLFWI image. The results of E-TLFWI show sharper salt boundaries on the velocity model, slightly improved RTM image, and more pronounced uplifts on the FWI image compared with the acoustic counterparts.

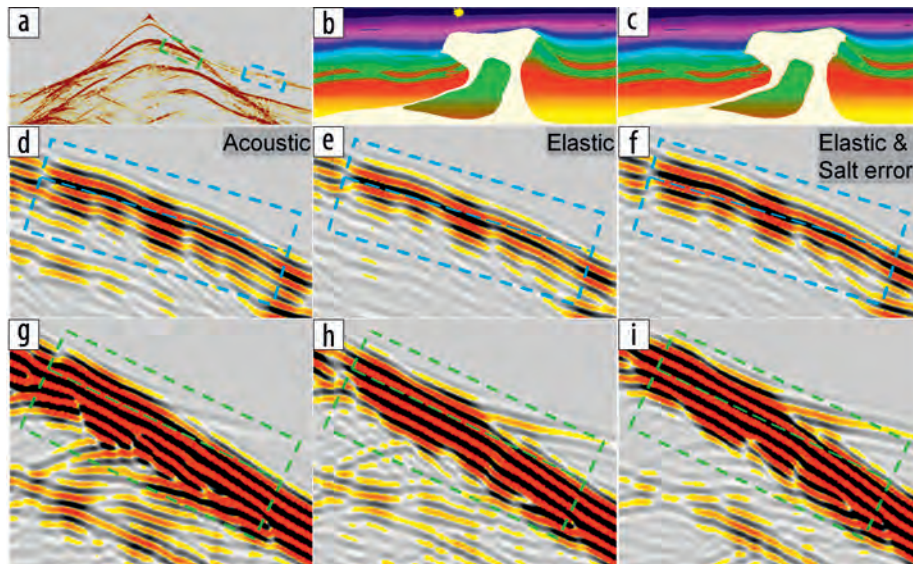


**Figure 11.** (a) Acoustic modeling data with a shot in the middle of (b) the BP 2004 model. (c) Model with slight salt errors compared with model (b). (d)–(f) Zoomed-in display of the diving waves shown within the blue rectangle in (a) by acoustic and elastic modeling of model (b), and elastic modeling of model (c). (g)–(i) Zoomed-in displays of the wide-angle reflections shown within the green rectangle in (a) by acoustic and elastic modeling of model (b), and elastic modeling of model (c).

- E-TLFWI can significantly reduce the salt halo typically observed in A-TLFWI models.
- With the exception of some improved focusing around salt complexities, RTM images using E-TLFWI velocity are qualitatively comparable to those using A-TLFWI velocity with some slight depth shifts.
- FWI images from E-TLFWI clearly show better event focusing, improved structural continuity, and higher S/N than those from A-TLFWI.

To better understand these observations, we compare acoustic and elastic modeling in the data domain using the BP 2004 velocity model (Billette and Brandsberg-Dahl, 2005). Acoustic modeling successfully simulates most events with traveltimes comparable to elastic modeling (Figures 11a and 11b). Reflections at the top of salt exhibit relatively large traveltime and phase differences, especially at middle to far offsets beyond the critical angle (Figures 11g and 11h), which we hypothesize are the origin of the salt halo that is observed in A-FWI models. The reflection waves mostly contribute to high-wavenumber construction, such as material interfaces, instead of overall model kinematics. Therefore, the sharpness of salt boundaries, where the elastic effects are strongest, highlights the differences between A-FWI and E-FWI velocity models. This large difference observed in reflection energy also explains why FWI images from A-TLFWI have much lower S/N than their elastic counterparts because the mismatch between the elastic input data and acoustic synthetic data can be translated easily into noise in the A-FWI model. Conversely, diving waves, the main driver for a low-wavenumber velocity update, exhibit a small traveltime difference between acoustic and elastic modeling. This is expected given the physical nature of diving waves. As a result, the kinematics of the A-FWI

and E-FWI models, which are mostly dictated by low wavenumbers, are similar if both A-FWI and E-FWI converge to their own optimal models. In addition, RTM as a migration approach is insensitive to the high-wavenumber details in the velocity model and is susceptible to other issues such as poor and uneven illumination. All these together explain why RTM images using A-TLFWI and E-TLFWI velocity are qualitatively comparable in terms of event focusing, structural continuity, and S/N, with just some slight depth shifts.

We further compare the modeling-engine-induced traveltime and phase differences with those caused by slight velocity errors in the salt model (Figure 11c) using the same elastic modeling engine. We observed that the difference caused by the latter is much larger for

both reflection and diving waves (Figures 11f and 11i). This means that A-FWI can be used first to fix most of the kinematic errors in the model and can be followed by E-FWI to correct high-order errors. This is attractive in a practical sense because it often takes multiple FWI passes to fix large model errors, especially when input data are suboptimal, which would be very expensive if E-FWI were required for this entire process.

**Evaluation of E-FWI.** RTM images using an E-FWI velocity model do not show much image uplift away from the salt complexity because of the comparable kinematics between A-FWI and E-FWI velocity models, the insensitivity of RTM image quality to the high-wavenumber information in the FWI velocity model, and the inconsistency of the modeling engine between E-FWI and A-RTM. Considering that migration images have been the final products of seismic imaging, these limited, or even disappointing, uplifts on image quality cast a shadow over the necessity to upgrade from A-FWI to E-FWI. Do we have more advanced imaging approaches that can better demonstrate the benefits of E-FWI?

One obvious candidate would be elastic RTM (E-RTM) that uses a modeling engine consistent with E-TLFWI. Figure 12 shows a comparison between A-RTM (Figure 12a) and E-RTM (Figure 12b) using the same E-TLFWI model. The E-RTM image shows improved truncation toward the salt boundary and better focused structure and event continuity in the subsalt. Those uplifts may not seem large given the comparable kinematics between the A-FWI and E-FWI models, but they can be significant for detailed reservoir interpretation. Nonetheless, the A-RTM and E-RTM images are still mostly comparable — almost identical in the sediment area and very similar in other areas away from the salt. This may be because the migration input data are muted to smaller angles and elastic effects are not as strong as those in FWI input data. The uplift seen in E-RTM is still far

less impressive than that in the E-FWI model, although both use an elastic modeling engine and have similar kinematics, if not the same due to the need to smooth the E-FWI velocity for E-RTM in some cases. We think this is due to three fundamental differences between RTM and FWI: (1) RTM takes processed primary data as input, while FWI takes the full-wavefield data including transmission and reflection waves and their multiples, which provides superior illumination over only primary reflections; (2) RTM adopts a single-scattering approximation, while FWI works with the full wavefield, which affords FWI the ability to better simulate and account for transmission losses; and (3) RTM uses an adjoint operator, while FWI is an iterative least-squares data-fitting process, which has the benefit of balancing illumination and mitigating migration artifacts. Least-squares RTM could be used to improve the result over RTM; however, least-squares RTM still carries the first two limitations listed above and, consequently, delivers results inferior to the FWI image (Huang et al., 2021; Wray et al., 2021), which is the normal derivative of the FWI velocity and inherently carries the benefit of FWI (Zhang et al., 2020; Huang et al., 2021; Wei et al., 2021).

The success of FWI imaging over conventional migration and LSM approaches makes it a potentially better tool to appreciate the full benefits of E-TLFWI. In particular, FWI images from E-TLFWI need to be substantially better than those from A-TLFWI to justify the greatly increased compute cost, given the benefit of E-TLFWI observed in conventional imaging products falls short of expectations in most cases. For all field data examples shown in this paper, FWI imaging demonstrates the significance of the elastic effects in FWI with better event focusing, improved structural continuity, and higher S/N (Figures 2, 7, and 10).

**Attributes beyond  $V_p$ .** Theoretically, E-TLFWI can be formulated to invert for elastic parameters. In practice, however, there are major challenges in multiparameter E-TLFWI, such as the strong coupling among different elastic parameters and insufficient constraints for all the parameters from the seismic data. Therefore, as of today,  $V_s$  and density are still mostly used as auxiliary models to assist a better inversion of  $V_p$ . In all of the examples shown in this paper, we only updated the  $V_p$  model while assuming empirical relationships between  $V_p$  and  $V_s$  and between  $V_p$  and density. However, more in-depth interpretation of rock properties for prospecting and reservoir analysis would require an accurate estimation of elastic parameters such as  $V_p$ ,  $V_s$ , and density. In conventional migrations, elastic parameters can be derived through amplitude variation with angle (AVA) inversion of the gathers output from migration. To achieve the same goal in the framework of FWI imaging, we could formulate the inversion to output the offset- or angle-dependent reflectivity. One straightforward approach is to divide the input data into

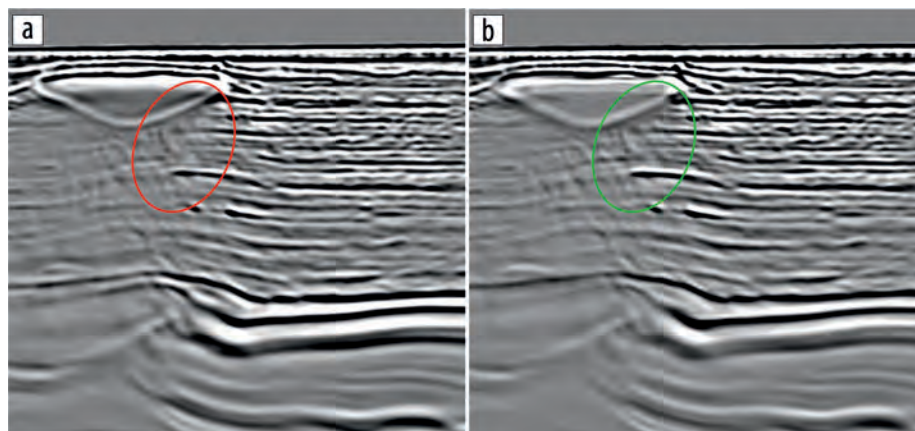


**Figure 12.** Section view of (a) 15 Hz A-RTM image with 15 Hz E-TLFWI velocity model and (b) 15 Hz E-RTM image with 15 Hz E-TLFWI velocity model. The E-RTM shows similar quality as the A-RTM except for slight improvements around salt boundaries and in the subsalt.

offset or subsurface angle groups and run FWI using each group respectively. Compared with conventional approaches, gathers obtained in this way automatically leverage the benefit of FWI imaging and, therefore, have the potential to offer more reliable AVA analysis for elastic parameter inversion. There is still more to explore in this approach, for instance whether the input separation in the time domain is acceptable, what role multiples and diving waves may play, and how to improve the affordability of FWI image gathers.

Ultimately, we would like to perform multiparameter E-FWI to directly invert for  $V_p$ ,  $V_s$ , and density (or other equivalent parametrizations). To achieve this goal, a few things need to be investigated: (1) optimizing the inversion scheme to best decouple different elastic parameters; (2) exploiting the full benefit of multiple-component data (e.g., pressure data and three-component velocity data from OBN surveys); and (3) designing sensors/surveys that can acquire data with more constraints for key elastic parameters.

## Conclusions

The synthetic example demonstrated that, although A-TLFWI with elastic input could construct a reasonable  $V_p$  model, it led to considerable salt halos, which smear the salt-sediment boundary and pose a problem for direct interpretation of the FWI velocity and FWI image around salt bodies. By taking elastic effects into account, E-TLFWI alleviated the salt halo problem and sharpened the salt-sediment boundary. Meanwhile, the E-TLFWI velocity model largely maintains the kinematics of the A-TLFWI, which are mainly determined by diving waves. The field data examples confirmed our findings and supported our observations in the synthetic tests that E-TLFWI significantly reduces the salt halo observed in A-TLFWI models. Moreover, the E-TLFWI velocity models also have clearer velocity contrasts and better details in the sediment and subsalt. While the improvements on the E-TLFWI velocity models are not well reflected in the quality of the corresponding RTM images, they are better appreciated through the E-FWI images, which show consistently better event focusing, improved structural continuity, and higher S/N than their acoustic counterparts. ■■

## Acknowledgments

We thank BP, Woodside Energy, and CGG for permission to publish this work. We are also grateful to many CGG colleagues for testing E-TLFWI on different data sets.

## Data and materials availability

Data associated with this research are confidential and cannot be released.

Corresponding author: [zhigang.zhang@cgg.com](mailto:zhigang.zhang@cgg.com)

## References

- Agudo, O. C., N. V. da Silva, G. Stronge, and M. Warner, 2020, Mitigating elastic effects in marine 3-D full-waveform inversion: *Geophysical Journal International*, **220**, no. 3, 2089–2104, <https://doi.org/10.1093/gji/ggz569>.
- Baysal, E., D. D. Kosloff, and J. W. C. Sherwood, 1983, Reverse time migration: *Geophysics*, **48**, no. 11, 1514–1524, <https://doi.org/10.1190/1.1441434>.
- Billette, F. J., and S. Brandsberg-Dhal, 2005, The 2004 BP velocity benchmark: 67<sup>th</sup> Conference & Exhibition, EAGE, Extended Abstracts, B035, <https://doi.org/10.3997/2214-4609-pdb.1.B035>.
- Claerbout, J. F., 1985, *Imaging the earth's interior*: Blackwell Science Inc.
- Claerbout, J. F., 1992, *Earth soundings analysis: Processing versus inversion*: Blackwell Science Inc.
- Huang, R., Z. Zhang, Z. Wu, Z. Wei, J. Mei, and P. Wang, 2021, Full-waveform inversion for full-wavefield imaging: Decades in the making: *The Leading Edge*, **40**, no. 5, 324–334, <https://doi.org/10.1190/tle40050324.1>.
- Lailly, P., 1983, The seismic inverse problem as a sequence of before stack migrations: *Conference on Inverse Scattering — Theory and Application*, SIAM, 206–220.
- Lewis, B., C. Brooks, M. Pfister, S. Michell, and G. Astvatsaturov, 2016, Efficient acquisition of deep-water node surveys: 86<sup>th</sup> Annual International Meeting, SEG, Expanded Abstracts, 92–96, <https://doi.org/10.1190/segam2016-13867668.1>.
- Liu, Y., X. Chang, D. Jin, R. He, H. Sun, and Y. Zheng, 2010, Reverse time migration of multiples for subsalt imaging: *Geophysics*, **76**, no. 5, WB209–WB216, <https://doi.org/10.1190/geo2010-0312.1>.
- Lu, S., N. D. Whitmore, A. A. Valenciano, and N. Chemingui, 2011, Imaging of primaries and multiples with 3D SEAM synthetic: 81<sup>st</sup> Annual International Meeting, SEG, Expanded Abstracts, 3217–3221, <https://doi.org/10.1190/1.3627864>.
- Michell, S., X. Shen, A. Brenders, J. Dellinger, I. Ahmed, and K. Fu, 2017, Automatic velocity model building with complex salt: Can computers finally do an interpreter's job?: 87<sup>th</sup> Annual International Meeting, SEG, Expanded Abstracts, 5250–5254, <https://doi.org/10.1190/segam2017-17778443.1>.
- Mora, P., and Z. Wu, 2018, Elastic versus acoustic inversion for marine surveys: *Geophysical Journal International*, **214**, no. 1, 596–622, <https://doi.org/10.1093/gji/ggy166>.
- Nemeth, T., C. Wu, and G. T. Schuster, 1999, Least-squares migration of incomplete reflection data: *Geophysics*, **64**, no. 1, 208–221, <https://doi.org/10.1190/1.1444517>.
- Nolte, B., F. Rollins, Q. Li, S. Dadi, S. Yang, J. Mei, and R. Huang, 2019, Salt velocity model building with FWI on OBN data: Example from Mad Dog, Gulf of Mexico: 89<sup>th</sup> Annual International Meeting, SEG, Expanded Abstracts, 1275–1279, <https://doi.org/10.1190/segam2019-3216777.1>.
- Plessix, R.-E., and T. Krupovnickas, 2021, Low-frequency, long-offset elastic waveform inversion in the context of velocity model building: *The Leading Edge*, **40**, no. 5, 342–347, <https://doi.org/10.1190/tle40050342.1>.
- Ren, D., X. He, S. Xu, F. Gao, F. Lin, and J. Mei, 2022, FWI for the complex Walker Ridge salt province using streamer data: Second International Meeting for Applied Geoscience & Energy, SEG/AAPG, Expanded Abstracts, 822–826, <https://doi.org/10.1190/image2022-3744364.1>.
- Schuster, G. T., 1993, Least-squares cross-well migration: 63<sup>rd</sup> Annual International Meeting, SEG, Expanded Abstracts, 110–113, <https://doi.org/10.1190/1.1822308>.
- Shen, X., I. Ahmed, A. Brenders, J. Dellinger, J. Etgen, and S. Michell, 2017, Salt model building at Atlantis with full-waveform inversion: 87<sup>th</sup> Annual International Meeting, SEG, Expanded Abstracts, 1507–1511, <https://doi.org/10.1190/segam2017-17738630.1>.
- Tarantola, A., 1984, Inversion of seismic reflection data in the acoustic approximation: *Geophysics*, **49**, no. 8, 1259–1266, <https://doi.org/10.1190/1.1441754>.
- Wang, P., A. Gomes, Z. Zhang, and M. Wang, 2016, Least-squares RTM: Reality and possibilities for subsalt imaging: 86<sup>th</sup> Annual International Meeting, SEG, Expanded Abstracts, 4204–4209, <https://doi.org/10.1190/segam2016-13867926.1>.
- Wang, P., Z. Zhang, J. Mei, F. Lin, and R. Huang, 2019, Full-waveform inversion for salt: A coming of age: *The Leading Edge*, **38**, no. 3, 204–213, <https://doi.org/10.1190/tle38030204.1>.
- Wei, Z., J. Mei, Z. Wu, Z. Zhang, R. Huang, and P. Wang, 2021, Unlocking unprecedented seismic resolution with FWI imaging: 82<sup>nd</sup> Annual Conference & Exhibition, EAGE, Extended Abstracts, <https://doi.org/10.3997/2214-4609.202113217>.
- Wong, M., B. Biondi, and S. Ronen, 2014, Imaging with multiples using least-squares reverse time migration: *The Leading Edge*, **33**, no. 9, 970–976, <https://doi.org/10.1190/tle33090970.1>.
- Wray, B., L. Zheng, F. Rozario, X. Zhang, N. Chazalnoel, and C. Mifflin, 2021, Paradigm shift: Recent advances in model building and imaging at Shenzhi: First International Meeting for Applied Geoscience & Energy, SEG/AAPG, Expanded Abstracts, 572–576, <https://doi.org/10.1190/segam2021-3580654.1>.
- Wu, Z., Z. Wei, Z. Zhang, J. Mei, R. Huang, and P. Wang, 2022, Elastic FWI for large impedance contrasts: Second International Meeting for Applied Geoscience & Energy, SEG/AAPG, Expanded Abstracts, 3686–3690, <https://doi.org/10.1190/image2022-w17-02.1>.
- Yang, Z., J. Hembd, H. Chen, and J. Yang, 2015, Reverse time migration of multiples: Applications and challenges: *The Leading Edge*, **34**, no. 7, 780–784, <https://doi.org/10.1190/tle34070780.1>.
- Yao, Y., H. Zhang, L. Hu, and C. Peng, 2020, Improving Mississippi Canyon images with ocean bottom node data: Challenges and surprises: 90<sup>th</sup> Annual International Meeting, SEG, Expanded Abstracts, 661–665, <https://doi.org/10.1190/segam2020-3423896.1>.
- Zhang, Z., J. Mei, F. Lin, R. Huang, and P. Wang, 2018, Correcting for salt misinterpretation with full-waveform inversion: 88<sup>th</sup> Annual International Meeting, SEG, Expanded Abstracts, 1143–1147, <https://doi.org/10.1190/segam2018-2997711.1>.
- Zhang, Z., Z. Wu, Z. Wei, J. Mei, R. Huang, and P. Wang, 2020, FWI imaging: Full-wavefield imaging through full-waveform inversion: 90<sup>th</sup> Annual International Meeting, SEG, Expanded Abstracts, 656–660, <https://doi.org/10.1190/segam2020-3427858.1>.